

Spectroscopic evidence of bilayer splitting and strong interlayer pairing in the superconductor $\text{KCa}_2\text{Fe}_4\text{As}_4\text{F}_2$

Dingsong Wu,^{1,2,*} Wenshan Hong,^{1,2,*} Chenxiao Dong,^{1,2,*} Xianxin Wu,^{1,3} Qiangtao Sui,^{1,2} Jianwei Huang,^{1,2} Qiang Gao,^{1,2} Cong Li,^{1,2} Chunyao Song,^{1,2} Hailan Luo,^{1,2} Chaohui Yin,^{1,2} Yu Xu,^{1,2} Xiangyu Luo,^{1,2} Yongqing Cai,^{1,2} Junjie Jia,^{1,2} Qingyan Wang,¹ Yuan Huang,¹ Guodong Liu,^{1,4} Shenjin Zhang,⁵ Fengfeng Zhang,⁵ Feng Yang,⁵ Zhimin Wang,⁵ Qinjun Peng,⁵ Zuyan Xu,⁵ Xianggang Qiu,^{1,2,4} Shiliang Li,^{1,2,4} Huiqian Luo,^{1,4,†} Jiangping Hu,^{1,2,4,‡} Lin Zhao,^{1,4,§} and X. J. Zhou^{Ⓢ1,2,4,6,||}

¹Beijing National Laboratory for Condensed Matter Physics, Institute of Physics, Chinese Academy of Sciences, Beijing 100190, China

²University of Chinese Academy of Sciences, Beijing 100049, China

³Department of Physics, Pennsylvania State University, University Park, Pennsylvania 16802, USA

⁴Songshan Lake Materials Laboratory, Dongguan, Guangdong 523808, China

⁵Technical Institute of Physics and Chemistry, Chinese Academy of Sciences, Beijing 100190, China

⁶Beijing Academy of Quantum Information Sciences, Beijing 100193, China



(Received 1 February 2020; revised manuscript received 6 May 2020; accepted 26 May 2020; published 12 June 2020)

We report high-resolution laser-based angle-resolved photoemission spectroscopy measurements on a newly discovered iron-based superconductor, $\text{KCa}_2\text{Fe}_4\text{As}_4\text{F}_2$ ($T_C = 33.5$ K), which consists of stacking FeAs blocks with two FeAs layers separated by insulating Ca_2F_2 blocks. Bilayer splitting effect is observed for the first time in iron-based superconductors that gives rise to a total of five holelike Fermi surface sheets observed around the Brillouin zone center. Band structure calculations reproduce the observed bilayer splitting by identifying interlayer interorbital interaction between the two FeAs layers within one FeAs block. All the holelike pockets around the zone center exhibit Fermi surface-dependent and nodeless superconducting gap. The gap functions with short-range antiferromagnetic fluctuations are proposed and the gap symmetry can be well understood when the interlayer pairing is considered. The particularly strong interlayer pairing is observed for one of the bands. Our observations provide key information on the role of interlayer coupling and the interlayer pairing in generating superconductivity in iron-based superconductors.

DOI: [10.1103/PhysRevB.101.224508](https://doi.org/10.1103/PhysRevB.101.224508)

I. INTRODUCTION

The newly discovered superconductor, $\text{ACa}_2\text{Fe}_4\text{As}_4\text{F}_2$ ($A = \text{K, Rb, and Cs, 12442}$), has attracted much attention because it provides a unique platform to study the superconductivity mechanism of the iron-based superconductors [1–10]. On the one hand, its crystal structure consists of bilayer FeAs blocks separated by insulating Ca_2F_2 blocks [1,2] [Fig. 1(a)]. The iron-based superconductors discovered so far can be classified into three main groups: one group consisting of single FeAs layer separated by insulating block layers [left panel in Fig. 1(b)] such as LaFeAsO system [11]; another group consisting of an infinite stack of FeAs/FeSe layers [right panel in Fig. 1(b)] such as FeSe [12], LiFeAs [13], and BaFe_2As_2 [14] systems. 12442 represents the third group that contains bilayer FeAs blocks separated by insulating Ca_2F_2 blocks [middle panel in Fig. 1(b)]. This is analogous to the double CuO_2 layers separated by insulating blocks in

$\text{Bi}_2\text{Sr}_2\text{CaCu}_2\text{O}_{8+\delta}$ (Bi2212) superconductor [15]. In Bi2212 , the interlayer interaction between the two equivalent CuO_2 planes in one structural unit leads to band splitting and the formation of two Fermi surface sheets (bonding and antibonding) [16–18] that have distinct superconducting gap [19]. In high-temperature cuprate superconductors, the interlayer coupling between the CuO_2 planes plays an important role in dictating superconductivity, as indicated by the sensitive dependence of the critical temperature (T_C) on the number of CuO_2 planes in one structural unit [20], but how the number of CuO_2 planes in one structural unit affects the superconductivity is still under debate. The iron-based superconductors are composed of stacking of the FeAs/FeSe layers; whether the interlayer coupling can cause similar band splitting and its effect on superconductivity remain unclear. 12442 provides an opportunity to investigate whether the interaction between the two FeAs layers within one bilayer FeAs block can produce a similar bilayer splitting and the effect of interlayer coupling on superconductivity in iron-based superconductors. On the other hand, band structure calculations indicate that there are six holelike pockets at the center of Brillouin zone (BZ) and four electronlike pockets at the zone corner [3,4]. The coexistence of such multiple Fermi surface sheets in one superconductor facilitates to study the relationship between the superconducting gap symmetry and the Fermi surface

*These authors contributed equally to this work.

†Corresponding author: hqluo@iphy.ac.cn

‡Corresponding author: jphu@iphy.ac.cn

§Corresponding author: lzhao@iphy.ac.cn

||Corresponding author: XJZhou@iphy.ac.cn

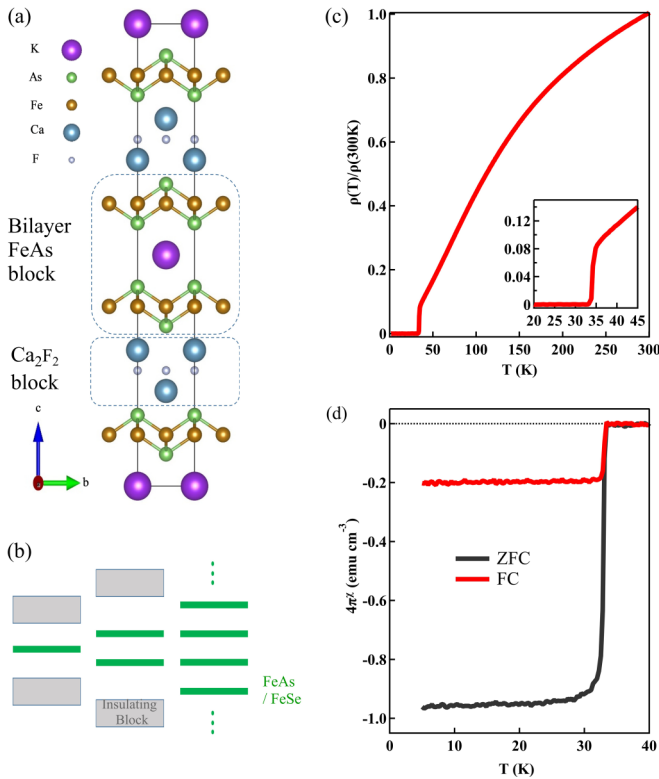


FIG. 1. Crystal structure and superconducting properties of K12442 superconductor with a T_c of 33.5 K. (a) Crystal structure consisting of bilayer FeAs block separated by insulating Ca_2F_2 block. (b) Schematic crystal structures of three groups of iron-based superconductors. Left: single FeAs/FeSe layer separated by insulating blocks; middle: double FeAs/FeSe layers separated by insulating blocks; right: infinite stacking of FeAs/FeSe layers. (c) Resistivity measurement within ab plane. The inset shows the data near the superconducting transition. (d) Magnetic susceptibility measurement with zero-field-cooling (ZFC) and field-cooling (FC) methods under a magnetic field of 0.9 Oe.

topology and to identify possible superconducting pairing model. The gap symmetry of 12442 reported so far has been controversial; muon-spin rotation experiment suggests it has a nodal gap [5,6] while optical and transport experiments point to a nodeless gap [7–9]. It becomes imperative to perform angle-resolved photoemission (ARPES) experiments on 12442 to directly measure its electronic structure and superconducting gap.

In this paper, we report the first high-resolution angle-resolved photoemission measurements on the band structure and superconducting gap of $\text{KC}_2\text{Fe}_4\text{As}_4\text{F}_2$ (K12442) superconductor. A complete Fermi surface topology is observed, which consists of five holelike pockets around the Brillouin zone center Γ point and tiny electronlike pockets around the zone corner M point. No Fermi surface nesting condition is satisfied between the electronlike pockets around M point and the holelike pockets around Γ point because of the apparent mismatch of their Fermi surface sizes. Band structure calculations indicate that these multiple bands around the zone center can be understood in terms of bilayer splitting where the interlayer interorbital interaction between the two FeAs layers

within one bilayer FeAs block gives rise to band splitting. This is similar to the bilayer splitting observed in Bi2212 superconductor [16–18]. Superconducting gap is measured on all the observed Fermi surface sheets and Fermi surface-dependent and nodeless superconducting gap is revealed. We found that the superconducting gap is dramatically different on one set of the bilayer-split holelike Fermi surface sheets; the maximal gap size shows up on one of the two sheets. The superconducting gap structure is understood by taking into account the interlayer pairing in the gap functions for the short-range antiferromagnetic fluctuations. Our results provide key insights in the interlayer interaction and the interlayer pairing in iron-based superconductors.

II. EXPERIMENT

High-quality single crystals of $\text{KC}_2\text{Fe}_4\text{As}_4\text{F}_2$ were grown by the KAs flux method [9]. The samples were characterized by electrical resistivity [Fig. 1(c)] and magnetic susceptibility [Fig. 1(d)] measurements and the measured T_c is 33.5 K with a narrow transition width of ~ 1 K. High-resolution angle-resolved photoemission measurements were carried out on our two laboratory-based ARPES systems. One is equipped with a hemispherical analyzer DA30 (Scienta Omicron) and a helium lamp with a photon energy of $h\nu = 21.218$ eV (helium I) [21]. The energy resolution was set at 10 meV for the Fermi surface measurement and 2.5 meV for the superconducting gap measurement. The other is equipped with a time-of-flight electron energy analyzer (ARToF 10k by Scienta Omicron) with a vacuum-ultraviolet (VUV) laser light source of $h\nu = 6.994$ eV [21,22]. This latest-generation ARToF-ARPES system is capable of measuring electronic structure covering two-dimensional momentum space (k_x, k_y) simultaneously. Another advantage of the ARToF analyzer is that it has much weaker nonlinearity effect so that the measured signal is intrinsic to the sample. The energy resolution was set at 1 meV and the angular resolution was $\sim 0.3^\circ$ corresponding to 0.004 \AA^{-1} momentum resolution at the photon energy of 6.994 eV. All the samples were cleaved *in situ* at low temperature of 13 K and measured in ultrahigh vacuum with a base pressure better than 5×10^{-11} mbar. The Fermi level was referenced by measuring on clean polycrystalline gold that was electrically connected to the sample or checked by the Fermi level of the measured sample in the normal state.

III. RESULTS AND DISCUSSIONS

Figure 2 shows the Fermi surface mapping and constant energy contours of K12442 by using both laser [Figs. 2(a)–2(f)] and helium lamp [Figs. 2(g)–2(i)] light sources. The corresponding band structures are shown in Fig. 3. The helium lamp measurement can cover a large momentum space, giving an overall Fermi surface of K12442 in the normal state measured at 38 K [Fig. 2(i)]. Three holelike pockets are clearly seen around Γ point, labeled as α , β , and γ in Fig. 2(i). Around M point, a tiny pocket (δ) can be identified, which is surrounded by four strong spots (ϵ) [Figs. 2(g) and 2(i)]. In the constant energy contour (CEC) at a binding energy of 20 meV, the tiny pocket around M disappears and the four strong spots change into four circular pockets

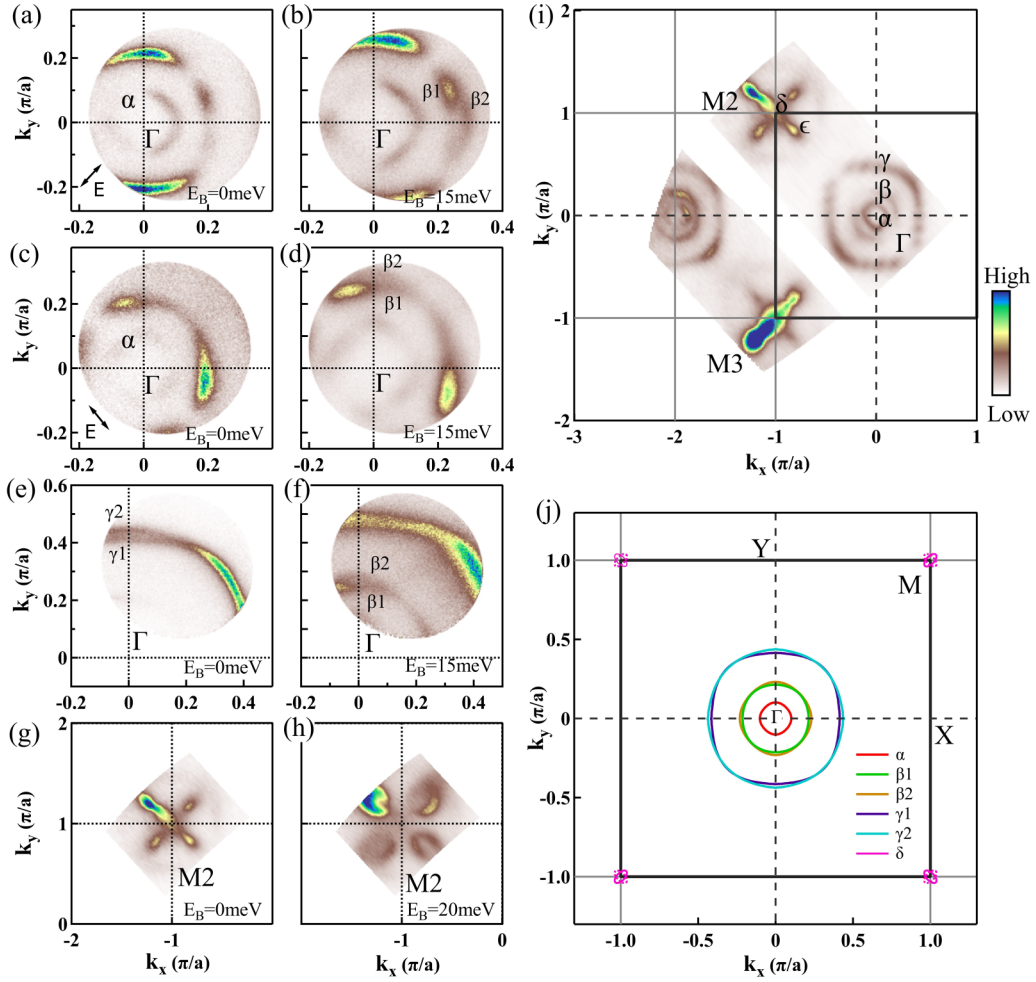


FIG. 2. Measured Fermi surface of K12442 superconductor. (a)–(h) Fermi surface mappings and constant energy contours covering different momentum space. The measurements around Γ point were carried out by using laser at 12–13 K for (a)–(f) and the measurements around M point were performed by using helium lamp at 38 K for (g)–(h). (a), (c), (e), (g) represents Fermi surface mappings and (b), (d), (f), (h) shows their corresponding constant energy contours at a binding energy of 15 meV (b), (d), (f) or 20 meV (h). They are obtained by integrating the spectral weight within a narrow energy window with respect to the Fermi level or the corresponding binding energies. The black double arrows in (a) and (c) represent E vector of the incident laser light. The observed Fermi surface sheets are marked by α , β_1 , β_2 , γ_1 , and γ_2 . The splitting of the β Fermi surface can be seen in (b), (d), and (f), and the splitting of the γ Fermi surface can be seen in (e). (i) Overall Fermi surface mapping consisting of three hole-like pockets (α , β , and γ) around Γ point and small electronlike pockets (δ) around M point measured at 38 K in the normal state with the helium lamp. (j) Summary of all the observed Fermi surface sheets obtained from the data in (a)–(i).

[Fig. 2(b)]. Such an evolution indicates the tiny pocket around M is electronlike while the four strong spots are holelike. In order to further examine on the Fermi surface topology around M , we carried out detailed momentum-dependent band structure measurements, as shown in Fig. 3(b). Electronlike bands near M can be seen from the momentum Cut 2 to Cut 4 in Fig. 3(b); their bottoms barely touch the Fermi level forming a tiny electronlike elliptical Fermi pocket as schematically shown in Fig. 2(j) (the other electron pocket is invisible due to matrix element effects and is also shown here). On the other hand, holelike inverse-parabolic bands are observed for the momentum cuts (Cuts 1, 3, and 5) crossing the four strong spots. The top of these bands is close to but does not cross the Fermi level to form Fermi surface, as seen from Cut 1 and Cut 5 in Fig. 3(b). The extended spectral

weight of the band tops at the Fermi level gives rise to four strong spots around M as observed in Figs. 2(g) and 2(i).

Laser ARToF-ARPES experiments were carried out to measure the Fermi surface of K12442 around Γ point. The capability of covering two-dimensional momentum space simultaneously with much higher-energy and momentum resolutions made it possible for us to reveal fine details on the electronic structure-band splitting in K12442. Two different laser polarizations were used in order to capture complete electronic structure by considering photoemission matrix element effects [23]. The measured Fermi surface mappings are shown in Figs. 2(a)–2(f) and the corresponding angle-dependent band structures are shown in Figs. 3(c)–3(h). All the three hole pockets are observed clearly with Figs. 2(a)–2(d) covering the inner (α) and middle (β) pockets while

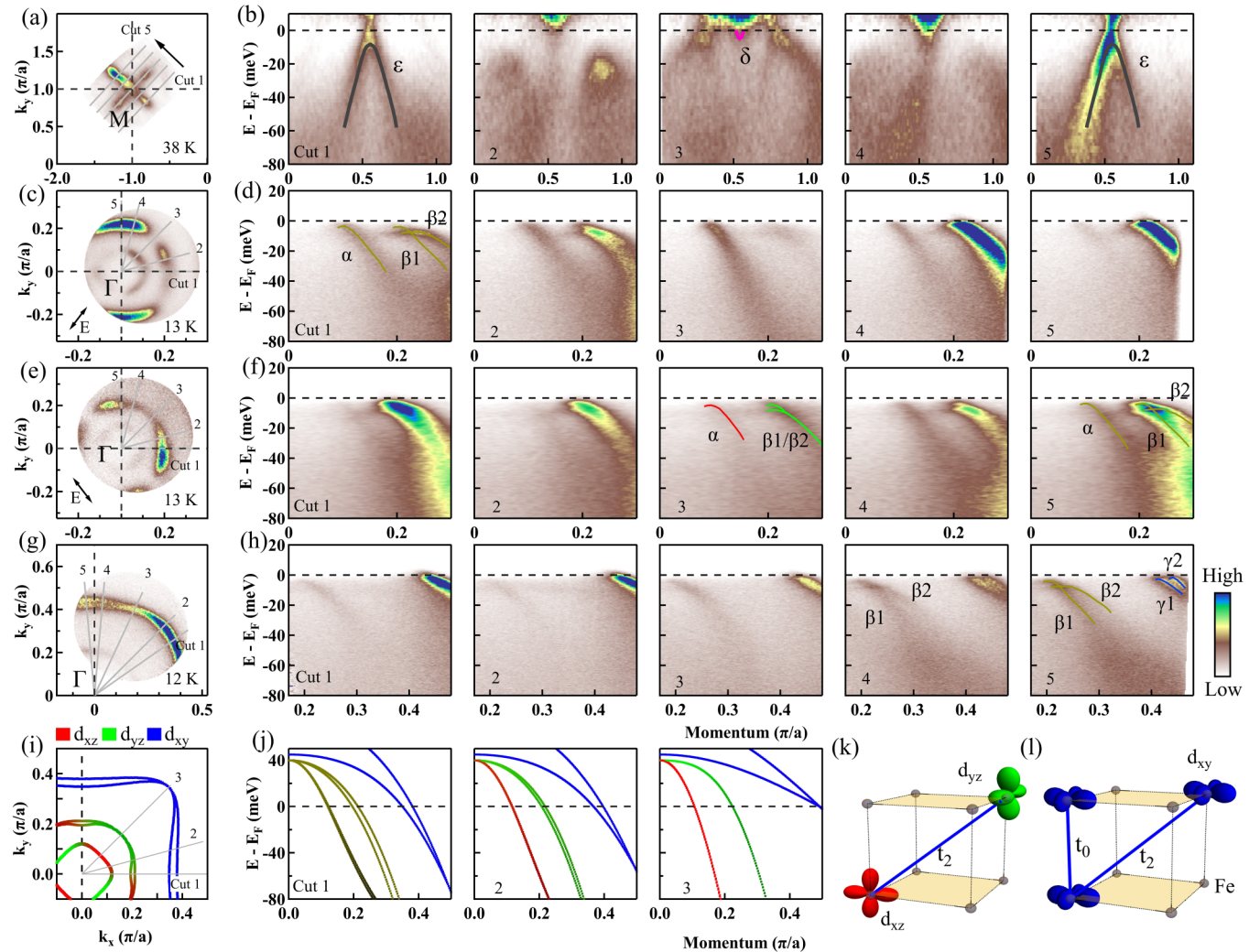


FIG. 3. Momentum-dependent band structures of K12442 superconductor and the comparison with band calculations. (a) Fermi surface mapping around M point measured by using helium lamp at a temperature of 38 K. The location of seven momentum cuts are marked by gray lines and their corresponding band structures are shown in (b). In order to see the features above the Fermi level, these spectral images are obtained by dividing the original data with the Fermi-Dirac distribution function. The ϵ band for the cuts 1 and 5 crossing the strong spots and the δ band for the Cut 3 crossing the M point are marked. Similar to (a), (c), (e), (g) show Fermi surface mappings around Γ point measured by using laser at 12–13 K in the superconducting state and the location of the momentum cuts. The corresponding band structures are shown in (d), (f), (h). The observed bands, α , β_1 and β_2 , γ_1 , and γ_2 , are marked in some of the images. (i) Calculated Fermi surface by considering the interlayer interaction between the two FeAs layers inside the bilayer FeAs block. The calculated momentum-dependent band structures are shown in (j); the location of the momentum cuts is marked as gray lines in (i). The d_{xz} , d_{yz} , and d_{xy} orbital components are represented by red, green, and blue colors, respectively. (k) Schematic of the main interlayer interorbital interaction involving the second-next-nearest neighbor hopping (t_2) and $d_{xz/yz}$ orbitals that causes the splitting of the β band. (l) Schematic of the main interlayer interorbital interaction involving the nearest- (t_0) and the second-nearest-neighbor (t_2) hoppings and d_{xy} orbital that causes the splitting of the γ band.

Figs. 2(e)–2(f) covering the middle (β) and outer (γ) pockets. Moreover, band splitting is observed for the β and γ bands. The β band splitting can be clearly seen from the constant energy contour in Fig. 2(b) where the β Fermi surface splits into two sheets β_1 and β_2 . It can also be seen directly from the measured band structure in Fig. 3: Cut 1 and Cut 2 in Fig. 3(d) in Fig. 3(f), especially clear in Cut 4 and Cut 5 in Fig. 3(h). The splitting is maximal along the $(0,0)$ - $(\pi,0)$ and $(0,0)$ - $(0,\pi)$ directions but minimal along the $(0,0)$ - (π,π) direction, resulting in two split β Fermi surface sheets as shown in Fig. 2(j). The γ band exhibits a similar splitting and the momentum dependence as the β band. The

γ band splitting can be observed from the Fermi surface mapping in Fig. 2(e) where the γ Fermi surface splits into two sheets γ_1 and γ_2 . It can also be seen directly from the measured band structure in Fig. 3: Cut 4 and Cut 5 in Fig. 3(h). The splitting is also maximal along $(0,0)$ - $(0,\pi)$ direction but minimal along the $(0,0)$ - (π,π) direction, resulting in two split γ Fermi surface sheets as shown in Fig. 2(j). Among all the measurements, we do not observe signature of band splitting for the α band. Overall, there are totally five hole pockets observed around Γ point and tiny electron pockets observed around M point [Fig. 2(j)]. The obtained hole concentration from the measured Fermi surface areas is 0.22 ± 0.03 hole/Fe

(the α pocket is considered twice in spite of its invisible band splitting). This concentration is consistent with the expected carrier concentration (0.25 hole/Fe) in stoichiometric K12442.

The multiple Fermi surface sheets observed in K12442 around Γ point can be understood in terms of bilayer splitting similar to the one observed in the cuprate superconductor Bi2212. Bi2212 consists of two CuO_2 planes in one structural unit separated by calcium (Ca); the structural unit is separated by insulating block layers. It is highly two dimensional because it exhibits a very strong anisotropy between the out-of-plane and in-plane resistivities [25]. Within the structural unit, the interaction between the two structurally equivalent CuO_2 planes gives rise to two Fermi surface sheets: bonding and antibonding ones [16–18,26–28]. In K12442, as shown in Fig. 1(a), the bilayer FeAs block consists of two FeAs layers separated by K; this bilayer unit is separated by insulating Ca_2F_2 block [1]. It also shows strong anisotropy between the out-of-plane and in-plane resistivities [10]. Within the bilayer FeAs block, the interaction between the two FeAs layers will cause the band splitting into two bands for each of the initial three bands in the single FeAs layer. The band splittings we observed in K12442 for the β and γ bands can be understood in this bilayer splitting picture, similar to that in Bi2212. It is not observed for the α band because the bilayer splitting is Fermi surface dependent and the splitting is too small to be detected for the α band.

We carried out band structure calculations to further understand the interaction between the two adjacent FeAs layers and the microscopic origin of the bilayer splitting in K12442. To simulate the band structure of K12442 system, we adopted the bilayer five-orbital tight-binding model with the interlayer hopping term

$$H_{\text{interlayer}} = 2t_2^{xz,yz} \sin kx \sin ky (c_{1,xz}^+ c_{2,yz} + c_{1,yz}^+ c_{2,xz} + c_{2,xz}^+ c_{1,yz} + c_{2,yz}^+ c_{1,xz}) + (t_0^{xy} + 2t_2^{xy} \cos kx \cos ky) (c_{1,xy}^+ c_{2,xy} + c_{2,xy}^+ c_{1,xy}), \quad (1)$$

where $c_{1,xz}^+$ is the creation operator of the orbit d_{xz} in layer 1, the rest operators are in the same way; $t_2^{xz,yz} = 20$ meV; $t_0^{xy} = -14$ meV; $t_2^{xy} = 15$ meV. Figure 3(i) shows the calculated Fermi surface; the corresponding calculated band structures along several momentum cuts are shown in Fig. 3(j). Compared with experimental data in Figs. 3(c)–3(h), the band splitting, its Fermi surface dependence, and the momentum dependence are well reproduced by the calculations. We found that the interlayer interorbital (d_{xz} and d_{yz}) hopping along the body diagonal (third-nearest-neighbor interaction t_2) in Fe lattice, as shown in Fig. 3(k), plays the dominant role in understanding the observed momentum-dependent band splitting of the β band. The α band shares similar orbital components and the interlayer interorbital interaction [Fig. 3(k)], however, its band splitting is invisible. It can be understood easily from Eq. (1). It is clear that, for the α and β bands comprising of d_{xz} and d_{yz} orbitals, the band splitting is proportional to $\sin kx \sin ky$. So the splitting of the α band is smaller than that of the β band because the α Fermi surface has a smaller radius. In order to understand the band splitting of the γ band, both

the nearest (t_0) and the third-nearest-neighbor (t_2) interlayer interorbital interactions have to be considered, as shown in Fig. 3(l).

The multiple Fermi surface sheets observed in K12442 provide a good opportunity to investigate the Fermi surface-dependent superconducting gap and their overall momentum dependence. We start by examining the temperature dependence of the superconducting gap on all the Fermi surface sheets, as shown in Fig. 4 and Fig. 5. Figures 4(b)–4(e) show the band structures measured at different temperatures along a momentum cut that covers α , β_1 and β_2 bands; the location of the momentum cut is marked in Fig. 4(a). These images are obtained by dividing the Fermi-Dirac distribution functions at their corresponding temperatures to facilitate investigation of the superconducting gap. In the normal state, all the observed bands smoothly cross the Fermi level [Fig. 4(b)]. In the superconducting state, the spectral weight at the Fermi level gets suppressed due to the opening of the superconducting gap [Figs. 4(c)–4(e)]. Figures 4(f)–4(h) show the photoemission spectra [energy distributed curves (EDCs)] measured at different temperatures on the Fermi momenta [marked by points in Fig. 4(a)] of α , β_1 , and β_2 bands, respectively. Sharp superconducting coherent peaks develop in the superconducting state for all the three bands. In order to quantitatively extract the superconducting gap size, the measured EDCs are symmetrized as shown in Figs. 4(i)–4(k). The gap size is obtained by fitting these symmetrized EDCs with a phenomenological formula [24] and the obtained gap size at different temperatures for the three bands is plotted in Fig. 5(i).

Figures 5(b)–5(c) show the band structures measured at different temperatures along another momentum cut that covers γ_1 and γ_2 bands, as well as β_1 and β_2 bands. The location of the momentum cut is marked in Fig. 5(a). Here the band splitting of the β band and γ band is particularly clear in the superconducting state [Fig. 5(c)]. These two images are also obtained by dividing the Fermi-Dirac distribution functions at their corresponding temperatures. In the normal state, the observed two sets of bands smoothly cross the Fermi level [Fig. 5(b)]. In the superconducting state, the spectral weight at the Fermi level gets suppressed due to the gap opening; it is more obvious for the β band than that for the γ band [Fig. 5(c)]. Figures 5(d)–5(e) show the EDCs measured at different temperatures on the Fermi momenta [marked by points in Fig. 5(a)] of γ_1 and γ_2 bands, respectively. The corresponding symmetrized EDCs are shown in Figs. 5(f)–5(g) and are fitted by the phenomenological formula [24]. The obtained superconducting gap size for the γ_1 and γ_2 bands is also included in Fig. 5(i). Figure 5(h) shows the temperature-dependent symmetrized EDCs on the tiny electron pocket around M point. The extracted gap size by fitting the symmetrized EDCs is plotted in Fig. 5(i). It can be found that superconducting gap opens on all the observed six bands and the gap size is different from each other [Fig. 5(i)]. With increasing temperature, all the gaps close at around the superconducting transition temperature T_C .

Now we come to the momentum dependence of the superconducting gap in this new superconductor K12442. Figure 6 shows the measured superconducting gap for all the five hole-like pockets around the Γ point. Taking advantage of the laser

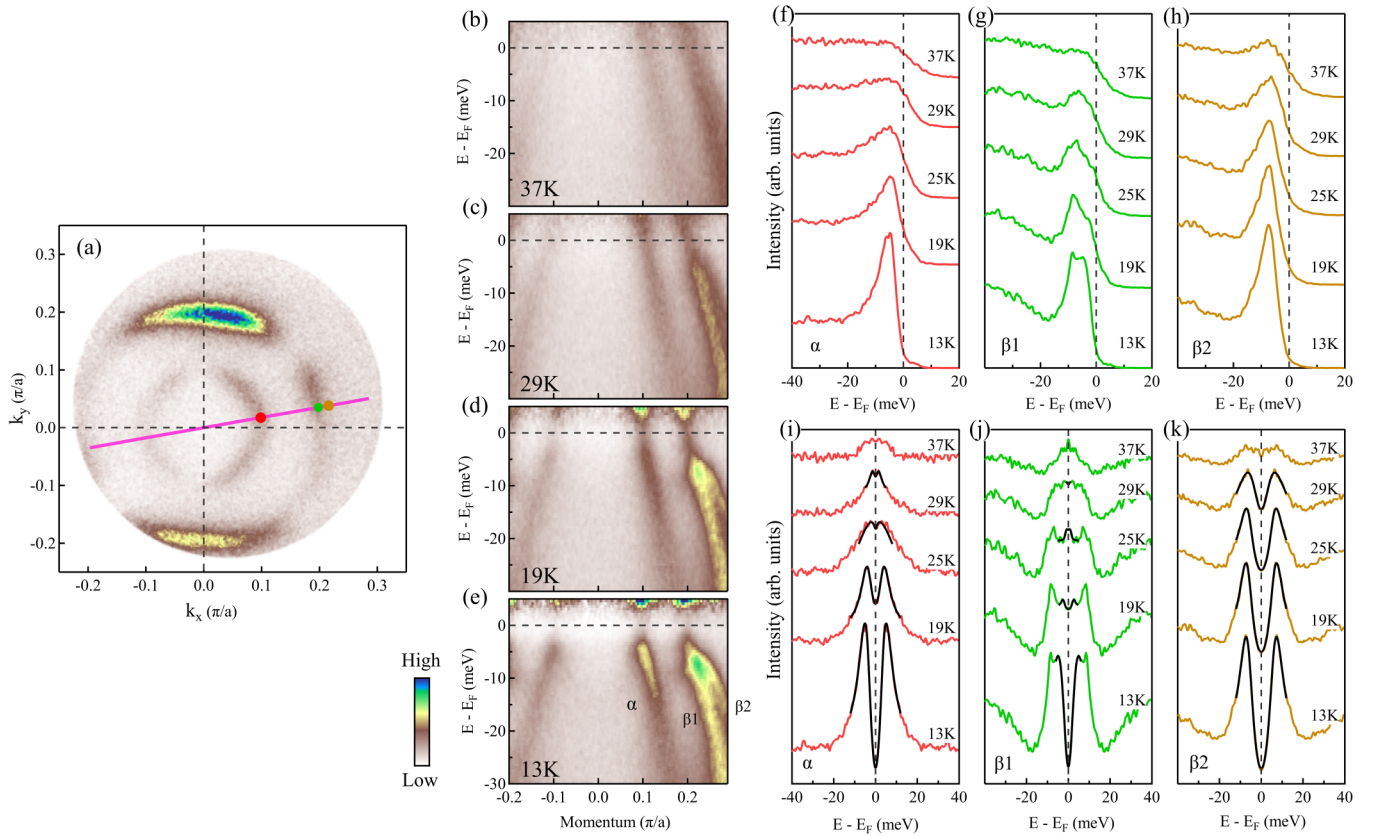


FIG. 4. Temperature dependence of the superconducting gap for the α , β_1 , and β_2 bands in K12442 superconductor. (a) Fermi surface mapping measured at 13 K by using laser. It covers α , β_1 , and β_2 Fermi pockets. The pink line marks the position of a momentum cut and the red, green and orange points represent the Fermi momentum position of the α , β_1 , and β_2 Fermi surface sheets. (b)–(e) Band structures measured at four different temperatures along the momentum cut shown in (a). The spectral images are divided by the Fermi-Dirac distribution function at their corresponding temperatures in order to highlight the superconducting gap. (f)–(h) Photoemission spectra (EDCs) measured at different temperatures for the three Fermi momenta, as indicated in (a), on α , β_1 , and β_2 pockets, respectively. The corresponding symmetrized EDCs are shown in (i)–(k).

ARToF-ARPES system in simultaneous two-dimensional momentum coverage, the superconducting gap can be extracted from dense Fermi momentum points measured under the same condition. Figures 6(f)–6(j) show the symmetrized EDCs measured along the five holelike Fermi surface sheets, α , β_1 , β_2 , γ_1 , and γ_2 , respectively, in the superconducting state. Their corresponding Fermi surface and Fermi momentum location along the Fermi surface are given in Figs. 6(a)–6(e). These symmetrized EDCs are fitted by the phenomenological formula [24] and the obtained superconducting gap size as a function of the Fermi surface angle for the α , β_1 , and β_2 , γ_1 and γ_2 is shown in Figs. 7(a)–7(c), respectively. Considering the fourfold symmetry of the crystal structure, we plot the superconducting gap distribution along the entire Fermi surface for the five holelike pockets around Γ and the electron pockets around M in Fig. 7(d). The measured superconducting gap in K12442 exhibits a number of characteristics. First, the superconducting gap shows an obvious Fermi surface dependence; its size varies among different Fermi surface sheets. The maximal gap size (~ 8 meV) appears on the β Fermi surface sheets whereas the minimal gap size appears on the γ sheets (~ 1 meV). Second, the superconducting gap is nearly isotropic; it shows a slight anisotropy along the β_2 and γ sheets. There is no gap node observed on all

the Fermi surface sheets. Because the electronic structure of K12442 is strongly two dimensional [3,4], the nodeless superconducting gap is expected to be on the entire Fermi surface although further measurements are needed to examine the k_z dependence of the superconducting gap. Third, for the β_1 and β_2 Fermi surface sheets, their gap size is dramatically different although their location in the momentum space is very close. We note that there is no evidence reported so far for the existence of nematicity in K12442 [1–10]. This is different from FeSe where nematicity is present below 90 K and nodal superconducting gap is reported [29,30].

K12442 has the largest number of observed Fermi surface sheets among all the iron-based superconductors discovered so far. With such multiple Fermi surface sheets, together with the detailed momentum-dependent superconducting gap measured on each sheet, K12442 provides an ideal system to examine on possible gap functions and explore on possible pairing mechanisms. Generally, there are two approaches to understand superconductivity of the iron-based superconductors [31,32]. In the Fermi surface nesting scenario of the itinerant picture [31–34], the electron scattering between the hole pockets around Γ and the electron pockets around M is proposed to be responsible for electron pairing. Such a mechanism was considered in $(\text{Ba}_{0.6}\text{K}_{0.4})\text{Fe}_2\text{As}_2$ [35] and

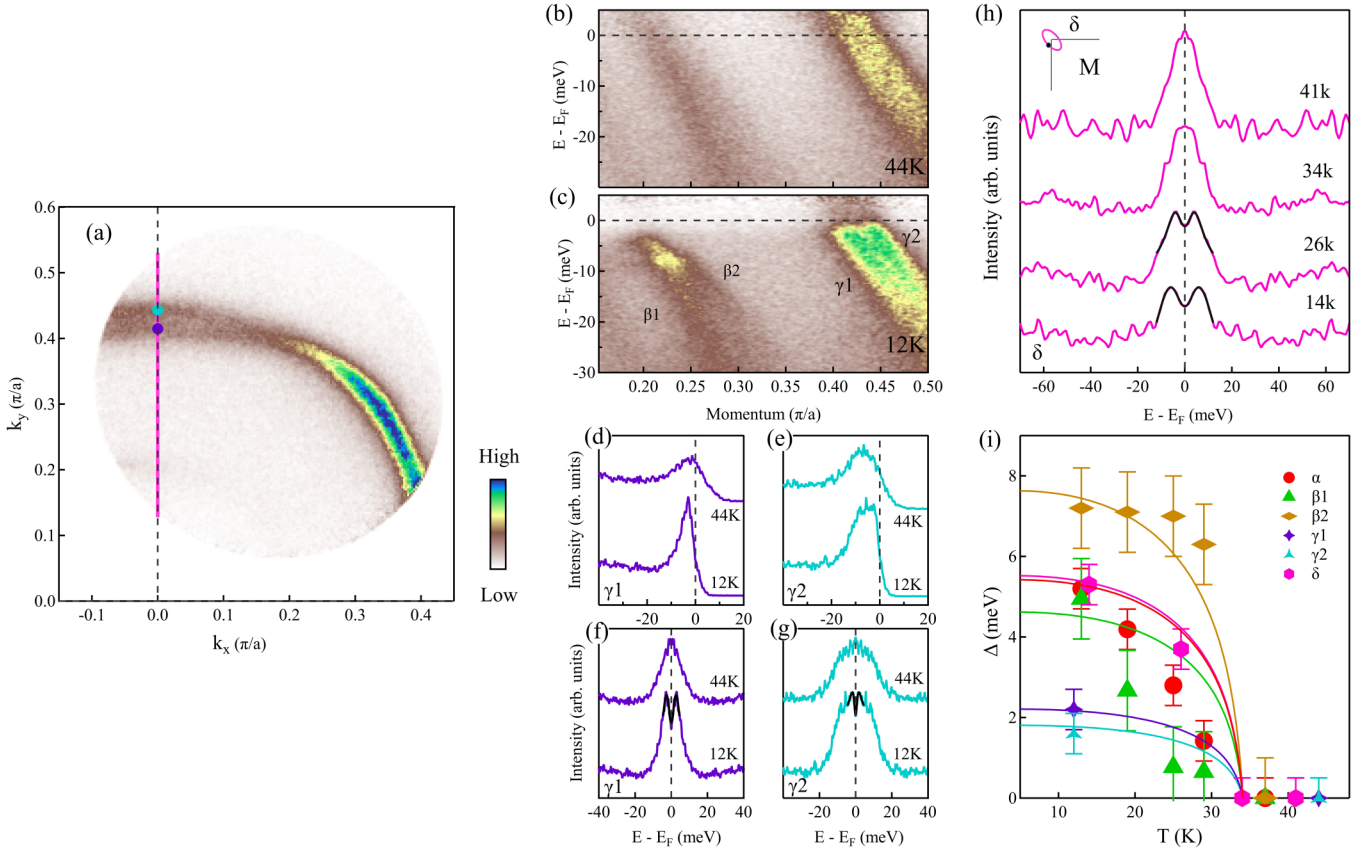


FIG. 5. Temperature dependence of the superconducting gap for the γ_1 , γ_2 bands and the electron pocket around the M point in K12442 superconductor. (a) Fermi surface mapping measured at 13 K by using laser. It covers β_1 , β_2 , γ_1 , and γ_2 Fermi pockets. The pink line marks the position of a momentum cut and the purple and blue points represent the Fermi momentum position of the γ_1 and γ_2 Fermi surface sheets. (b)–(c) Band structures measured at two different temperatures along the momentum cut shown in (a). The spectral images are also divided by the Fermi-Dirac distribution function at their corresponding temperatures. (d)–(e) EDCs measured at different temperatures for the two Fermi momenta, as indicated in (a), on γ_1 and γ_2 pockets, respectively. The corresponding symmetrized EDCs are shown in (f)–(g). (h) Symmetrized EDCs at the Fermi momentum of the tiny electron pocket around M point measured at different temperatures by using helium lamp. All the symmetrized EDCs in Fig. 4 and Fig. 5 are fitted by the phenomenological formula [24]; the obtained superconducting gap size as a function of temperature for all the six Fermi surface sheets is plotted in (i). The solid lines represent curves corresponding to the BCS gap function. Superconducting gap opens on all the Fermi surface sheets in the superconducting state and closes at the superconducting transition temperature.

CaKFe₄As₄ [36] superconductors. The possibility of this nesting-driven pairing mechanism can be ruled out in K12442 because of the apparent Fermi surface size mismatch between the hole pockets around Γ and the electron pockets around M , as seen in Fig. 2(j).

For the strong coupling approach [31,32,37], the pairing of electrons occurs because of a short-range interaction. Here, we consider the order parameter of β band in the single FeAs layer. The major orbit composition of β band is given as:

$$\psi_{\beta}(k) = e^{i\alpha(k)}[\cos\theta\psi_{xz}(k) - \sin\theta\psi_{yz}(k)], \quad (2)$$

where $\alpha(k)$ is the gauge of the β band; ψ_{xz} and ψ_{yz} represent wave functions of the d_{xz} and d_{yz} orbitals; $\theta = \arctan \frac{k_x}{k_y}$. Obviously, the absolute value of the intraband order parameter in β band is

$$\Delta_{\beta}(k) = (\cos\theta)^2\Delta_{xz}(k) + (\sin\theta)^2\Delta_{yz}(k) - \sin\theta\cos\theta\Delta_{xz,yz}(k), \quad (3)$$

where Δ_{xz} and Δ_{yz} are the order parameters of the d_{xz} and d_{yz} orbitals, respectively; $\Delta_{xz,yz}(k)$ is the order parameter of the interorbital pairs, given as:

$$\Delta_{xz,yz}(k) = \langle \psi_{xz}(k)\psi_{yz}(-k) + \psi_{xz}(-k)\psi_{yz}(k) \rangle. \quad (4)$$

Then, we consider the intraorbital order parameter of β_1 band and β_2 band in the K12442 system. In a familiar way, the main orbital composition of β_1 and β_2 bands can be calculated based on the above tight-binding model:

$$\begin{aligned} \psi_{\beta_1}(k) &= \frac{\sqrt{2}}{2}e^{i\alpha_1(k)}[\cos\theta\psi_{1,xz}(k) - \sin\theta\psi_{1,yz}(k) \\ &\quad + \cos\theta\psi_{2,xz}(k) - \sin\theta\psi_{2,yz}(k)] \\ \psi_{\beta_2}(k) &= \frac{\sqrt{2}}{2}e^{i\alpha_2(k)}[\cos\theta\psi_{1,xz}(k) - \sin\theta\psi_{1,yz}(k) \\ &\quad - \cos\theta\psi_{2,xz}(k) + \sin\theta\psi_{2,yz}(k)], \end{aligned} \quad (5)$$

where $\alpha_1(k)$ and $\alpha_2(k)$ are the gauge of β_1 and β_2 bands, respectively; $\psi_{1,xz}(k)$ represents the wave function of d_{xz} in

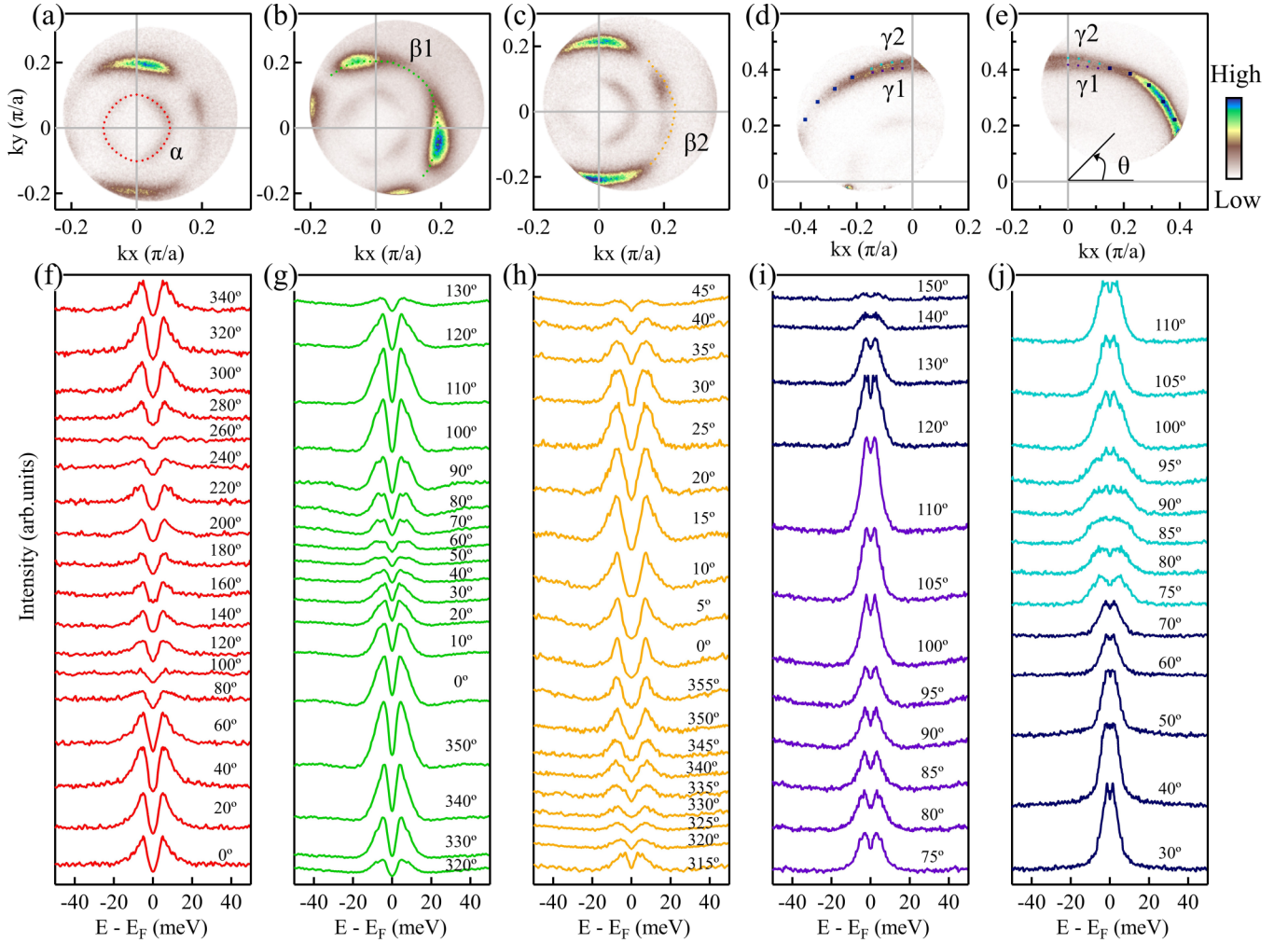


FIG. 6. Momentum-dependent symmetrized EDCs of K12442 superconductor. (a)–(e) Fermi surface mappings measured at low temperature of 12–13 K. (f)–(j) Symmetrized EDCs along the α , β_1 , β_2 , γ_1 , and γ_2 Fermi surface sheets, respectively, as a function of the Fermi surface angle θ . The Fermi surface angle θ is defined with respect to the Γ -X direction, as shown in (e). The location of the Fermi momenta is also marked in the corresponding Fermi surface mappings. The symmetrized EDCs of γ_1 and γ_2 in (i) and (j) are extracted from both (d) and (e).

layer 1, the rest ψ 's are in a familiar way; $\theta = \arctan \frac{k_x}{k_y}$. Based on the above equations, we obtain the absolute value of the order parameter in β_1 and β_2 bands:

$$\begin{aligned} \Delta_{\beta_1}(k) &= \Delta_{\beta}(k) + \Delta_{\text{interlayer}}(k) \\ \Delta_{\beta_2}(k) &= \Delta_{\beta}(k) - \Delta_{\text{interlayer}}(k), \end{aligned} \quad (6)$$

where the $\Delta_{\text{interlayer}}(k)$ is the order parameter of the superconducting pairs between the two different layers:

$$\begin{aligned} \Delta_{\text{interlayer}}(k) &= (\cos \theta)^2 \langle \psi_{1,xz}(k) \psi_{2,xz}(-k) + \psi_{1,xz}(-k) \psi_{2,xz}(k) \rangle \\ &+ (\sin \theta)^2 \langle \psi_{1,yz}(k) \psi_{2,yz}(-k) + \psi_{1,yz}(-k) \psi_{2,yz}(k) \rangle \\ &- \sin \theta \cos \theta \langle \psi_{1,xz}(k) \psi_{2,yz}(-k) + \psi_{1,xz}(-k) \psi_{2,yz}(k) \rangle \\ &+ \psi_{2,xz}(k) \psi_{1,yz}(-k) + \psi_{2,xz}(-k) \psi_{1,yz}(k). \end{aligned} \quad (7)$$

Referring to $(\text{Ba}_{0.6}\text{K}_{0.4})\text{Fe}_2\text{As}_2$ [38], and considering the discussions above, we propose a generalized s -wave gap function for K12442: $\Delta_s = |\frac{1}{2} \Delta_0 (\cos k_x + \cos k_y) \pm \frac{1}{2} \Delta_z \cos \frac{k_x}{2} \cos \frac{k_y}{2}|$ in 2-Fe unit cell, where the intralayer pairing Δ_0 originates

from the intralayer next-nearest-neighbor exchange coupling J_2 and the interlayer pairing Δ_z comes from interlayer exchange coupling J_z [see inset in Fig. 7(f)]. First, Δ_z has to be considered in order to understand the dramatic difference of the superconducting gap for the two β split bands. Second, if we consider the interlayer pairing but assume band-independent Δ_0 and Δ_z , clear deviation still exists, as shown in Fig. 7(e), particularly for the β_2 and γ_1 bands. Only when we consider the interlayer pairing and band-dependent Δ_0 and Δ_z can we fit the observed gap well, as shown in Fig. 7(f). The Δ_0 and Δ_z for different Fermi surface sheets are thus obtained, as also included in Fig. 7(f). We find that the intralayer pairing shows a clear Fermi surface dependence; it is strongest for the β band ($\Delta_0 = 6.8$ meV) while weakest for the γ band ($\Delta_0 = 3.3$ meV). Furthermore, the interlayer pairing also exhibits a Fermi surface dependence, which is also strongest for the β band ($\Delta_z = 4$ meV). The interlayer pairing for the β band is stronger than that observed in $(\text{Ba}_{0.6}\text{K}_{0.4})\text{Fe}_2\text{As}_2$ ($\Delta_z = 2.07$ meV) [38] and is the strongest discovered so far in iron-based superconductors.

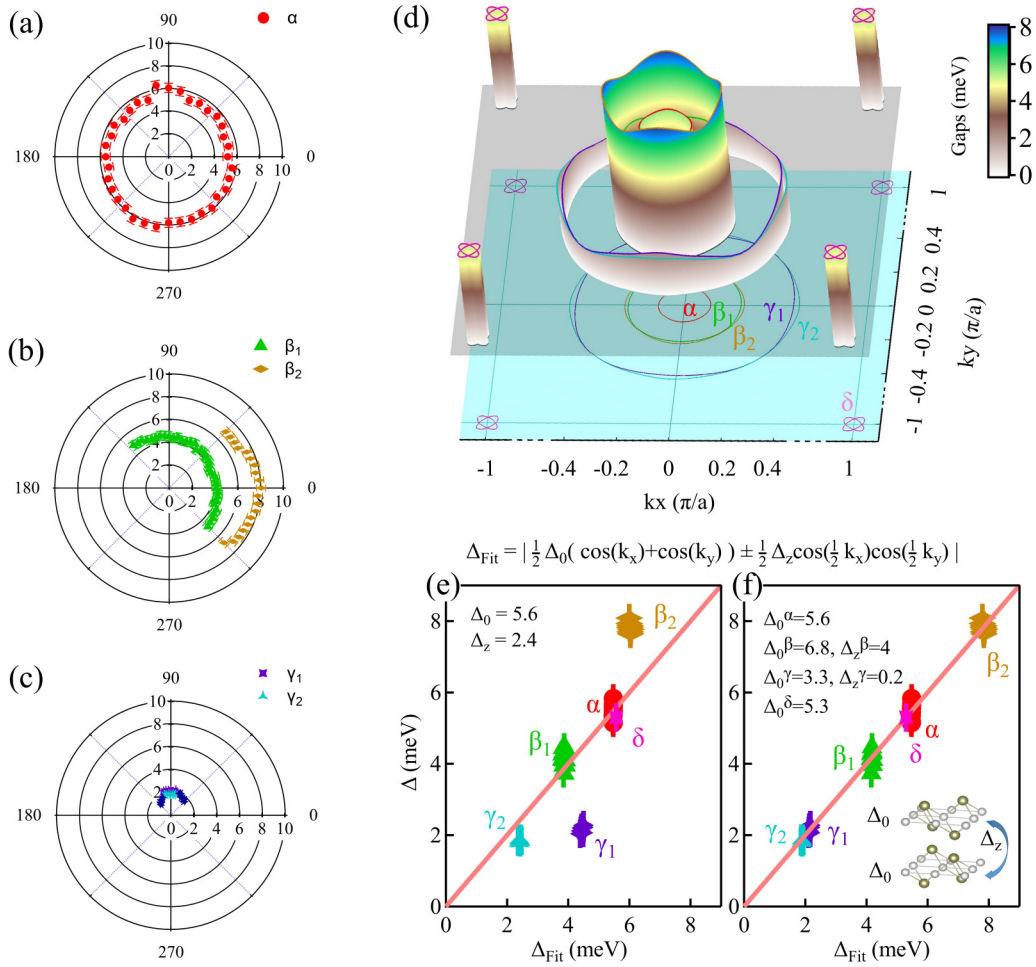


FIG. 7. Momentum-dependent superconducting gap of K12442 superconductor. All the symmetrized EDCs in Figs. 5(f)–5(j) are fitted by the phenomenological formula [24]. (a)–(c) The obtained superconducting gap size as a function of the Fermi surface angle for the α , β_1 , and β_2 , γ_1 and γ_2 Fermi surface sheets, respectively, as polar graphs. (d) Three-dimensional plot of the superconducting gap on the five observed hole pockets around Γ point and the tiny electron pockets around M point. The corresponding Fermi surface is shown at the bottom. (e) Superconducting gap size on various Fermi surface sheets as a function of $\Delta_s = |\frac{1}{2} \Delta_0 (\cos k_x + \cos k_y) \pm \frac{1}{2} \Delta_z \cos \frac{k_x}{2} \cos \frac{k_y}{2}|$ by considering Fermi surface-independent intralayer pairing (Δ_0) and interlayer pairing (Δ_z). (f) Same as (e) but considering Fermi surface-dependent intralayer pairing (Δ_0) and interlayer pairing (Δ_z).

IV. CONCLUSION

In summary, we carried out high-resolution laser ARPES measurements on a newly discovered iron-based superconductor, $\text{KCa}_2\text{Fe}_4\text{As}_4\text{F}_2$. In total five holelike Fermi surface sheets around Γ point and tiny electronlike pockets around M point are observed. The bilayer splitting effect is clearly identified, which represents the first case discovered in iron-based superconductors. It mainly originates from the interlayer interorbital interactions. Fermi surface-dependent superconducting gap is observed and no node exists on the observed Fermi surface. In particular, the superconducting gap on the two split β bands is dramatically different and the maximal gap size appears on one of the bands. The observed Fermi surface topology clearly rules out the Fermi surface nesting picture in understanding the superconductivity in $\text{KCa}_2\text{Fe}_4\text{As}_4\text{F}_2$. Instead, the measured superconducting gap is consistent with the gap functions considering short-range and band-dependent pairing; the particularly strong interlayer pairing is observed for the β band. Our results provide key

insights into the role of the interlayer interaction and interlayer pairing played in dictating the superconductivity in iron-based superconductors.

ACKNOWLEDGMENTS

This work is supported by the National Natural Science Foundation of China (Grants No. 11888101, No. 11534007, No. 11822411, No. 11374011, No. 11922414, and No. 11874405), the National Key Research and Development Program of China (Grants No. 2016YFA0300300, No. 2017YFA0302900, No. 2018YFA0704200, and No. 2019YFA0308000), the Strategic Priority Research Program (B) of the Chinese Academy of Sciences (Grant No. XDB25000000), the Research Program of Beijing Academy of Quantum Information Sciences (Grant No. Y18G06) and the Youth Innovation Promotion Association of CAS (Grants No. 2017013, No. 2016004, and No. 2019007).

X.J.Z., L.Z., and D.S.W. proposed and designed the research. W.S.H., H.Q.L. and S.L.L. contributed in sample growth. D.S.W., J.W.H., Q.G., C.L., C.Y.S., H.L.L., C.H.Y., Y.X., X.Y.L., Y.Q.C., J.J.J., Q.Y.W., Y.H., G.D.L., S.J.Z., F.F.Z., F.Y., Z.M.W., Q.J.P., Z.Y.X., L.Z., and X.J.Z. contributed to the development and maintenance of the ARPES systems and related software development. Q.T.S., X.G.Q.,

W.S.H., H.Q.L., and D.S.W. contributed to the magnetic and resistivity measurements. D.S.W. carried out the ARPES experiment with L.Z.. D.S.W., L.Z., and X.J.Z. analyzed the data. C.X.D., X.X.W., and J.P.H. contributed to the band structure calculations and theoretical analysis. D.S.W., L.Z., and X.J.Z. wrote the paper with C.X.D., X.X.W., and J.P.H.. All authors participated in discussion and comment on the paper.

- [1] Z. C. Wang, C. Y. He, S. Q. Wu, Z. T. Tang, Y. Liu, A. Ablimit, C. M. Feng, and G. H. Cao, Superconductivity in $\text{KCa}_2\text{Fe}_4\text{As}_4\text{F}_2$ with separate double Fe_2As_2 layers, *J. Am. Chem. Soc.* **138**, 7856 (2016).
- [2] Z. C. Wang, C. Y. He, Z. T. Tang, S. Q. Wu, and G. H. Cao, Crystal structure and superconductivity at about 30 K in $\text{ACa}_2\text{Fe}_4\text{As}_4\text{F}_2$ ($A = \text{Rb}, \text{Cs}$), *Sci. China Mater.* **60**, 83 (2017).
- [3] G. T. Wang, Z. W. Wang, and X. B. Shi, Self-hole-doping induced superconductivity in $\text{KCa}_2\text{Fe}_4\text{As}_4\text{F}_2$, *Europhys. Lett.* **116**, 37003 (2016).
- [4] J. Ishida, S. Imura, and H. Hosono, Effects of disorder on the intrinsically hole-doped iron-based superconductor $\text{KCa}_2\text{Fe}_4\text{As}_4\text{F}_2$ by cobalt substitution, *Phys. Rev. B* **96**, 174522 (2017).
- [5] F. K. K. Kirschner, D. T. Adroja, Z. C. Wang, F. Lang, M. Smidman, P. J. Baker, G. H. Cao, and S. J. Blundell, Two-gap superconductivity with line nodes in $\text{CsCa}_2\text{Fe}_4\text{As}_4\text{F}_2$, *Phys. Rev. B* **97**, 060506(R) (2018).
- [6] M. Midman, F. K. K. Kirschner, D. T. Adroja, A. D. Hillier, F. Lang, Z. C. Wang, G. H. Cao, and S. J. Blundell, Nodal multigap superconductivity in $\text{KCa}_2\text{Fe}_4\text{As}_4\text{F}_2$, *Phys. Rev. B* **97**, 060509(R) (2018).
- [7] B. Xu, Z. C. Wang, E. Sheveleva, F. Lyzwa, P. Marsik, G. H. Cao, and C. Bernhard, Band-selective clean-limit and dirty-limit superconductivity with nodeless gaps in the bilayer iron-based superconductor $\text{CsCa}_2\text{Fe}_4\text{As}_4\text{F}_2$, *Phys. Rev. B* **99**, 125119 (2019).
- [8] Y. Y. Huang, Z. C. Wang, Y. J. Yu, J. M. Ni, Q. Li, E. J. Cheng, G. H. Cao, and S. Y. Li, Multigap nodeless superconductivity in $\text{CsCa}_2\text{Fe}_4\text{As}_4\text{F}_2$ probed by heat transport, *Phys. Rev. B* **99**, 020502(R) (2019).
- [9] T. Wang, J. N. Chu, J. X. Feng, L. L. Wang, X. G. Xu, W. Li, H. H. Wen, X. S. Liu, and G. Mu, Low temperature specific heat of the 12442-Type $\text{KCa}_2\text{Fe}_4\text{As}_4\text{F}_2$ single crystals, *Sci. China-Phys. Mech. Astron.* **63**, 297412 (2020).
- [10] Z. C. Wang, Y. Liu, S. Q. Wu, Y. T. Shao, Z. Ren, and G. H. Cao, Giant anisotropy in superconducting single crystals of $\text{CsCa}_2\text{Fe}_4\text{As}_4\text{F}_2$, *Phys. Rev. B* **99**, 144501 (2019).
- [11] Y. Kamihara, T. Watanabe, M. Hirano, and H. Hosono, Iron-based layered superconductor $\text{La}[\text{O}_{1-x}\text{F}_x]\text{FeAs}$ ($x=0.05-0.12$) with $T_c=26$ K, *J. Am. Chem. Soc.* **130**, 3296 (2008).
- [12] F. Hsu, J. Luo, K. Yeh, T. Chen, T. Huang, P. M. Wu, Y. Lee, Y. Huang, Y. Chu, D. Yan, and M. Wu, Superconductivity in the PbO-type structure α -FeSe, *Proc. Natl. Acad. Sci. USA* **105**, 14262 (2008).
- [13] X. C. Wang, Q. Q. Liu, Y. X. Lv, W. B. Gao, L. X. Yang, R. C. Yu, F. Y. Li, and C. Q. Jin, The superconductivity at 18 K in LiFeAs system, *Solid State Commun.* **148**, 538 (2008).
- [14] M. Rotter, M. Tegel, D. Johrendt, I. Schellenberg, W. Hermes, and R. Pottgen, Spin-density-wave anomaly at 140 K in the ternary iron arsenide BaFe_2As_2 , *Phys. Rev. B* **78**, 020503 (2008).
- [15] B. Raveau, C. Michel, M. Hervieu, and D. Groult, *Crystral Chemistry of High-Tc Superconducting Copper Oxides* (Springer-Verlag, Berlin, 1991).
- [16] P. V. Bogdanov, A. Lanzara, X. J. Zhou, S. A. Kellar, D. L. Feng, E. D. Lu, H. Eisaki, J. I. Shimoyama, K. Kishio, Z. Hussain, and Z. X. Shen, Photoemission study of Pb doped $\text{Bi}_2\text{Sr}_2\text{CaCu}_2\text{O}_8$: A fermi surface picture, *Phys. Rev. B* **64**, 180505(R) (2001).
- [17] D. L. Feng, N. P. Armitage, D. H. Lu, A. Damascelli, J. P. Hu, P. Bogdanov, A. Lanzara, F. Ronning, K. M. Shen, H. Eisaki, C. Kim, Z. X. Shen, J. Shimoyama, and K. Kishio, Bilayer Splitting in the Electronic Structure of Heavily Overdoped $\text{Bi}_2\text{Sr}_2\text{CaCu}_2\text{O}_{8+\delta}$, *Phys. Rev. Lett.* **86**, 5550 (2001).
- [18] Y. D. Chuang, A. D. Gromko, A. Fedorov, Y. Aiura, K. Oka, Y. Ando, H. Eisaki, S. I. Uchida, and D. S. Dessau, Doubling of the Bands in Overdoped $\text{Bi}_2\text{Sr}_2\text{CaCu}_2\text{O}_{8+\delta}$: Evidence for c-axis Bilayer Coupling, *Phys. Rev. Lett.* **87**, 117002 (2001).
- [19] P. Ai, Q. Gao, J. Liu, Y. X. Zhang, C. Li, J. W. Huang, C. Y. Song, H. T. Yan, L. Zhao, G. D. Liu, G. D. Gu, F. F. Zhang, F. Yang, Q. J. Peng, Z. Y. Xu, and X. J. Zhou, Distinct superconducting gap on two bilayer-split fermi surface sheets in $\text{Bi}_2\text{Sr}_2\text{CaCu}_2\text{O}_{8+\delta}$ superconductor, *Chin. Phys. Lett.* **36**, 067402 (2019).
- [20] H. Eisaki, N. Kaneko, D. L. Feng, A. Damascelli, P. K. Mang, K. M. Shen, Z. X. Shen, and M. Greven, Effect of chemical inhomogeneity in bismuth-based copper oxide superconductors, *Phys. Rev. B* **69**, 064512 (2004).
- [21] X. J. Zhou, S. L. He, G. D. Liu, L. Zhao, L. Yu, and W. T. Zhang, New developments in laser-based photoemission spectroscopy and its scientific applications: A key issues review, *Rep. Prog. Phys.* **81**, 062101 (2018).
- [22] Y. Zhang, C. L. Wang, L. Yu, G. D. Liu, A. J. Liang, J. W. Huang, S. M. Nie, X. Sun, Y. X. Zhang, B. Shen, J. Liu, H. M. Weng, L. X. Zhao, G. F. Chen, X. W. Jia, C. Hu, Y. Ding, W. J. Zhao, Q. Gao, C. Li, S. L. He, L. Zhao, F. F. Zhang, S. J. Zhang, F. Yang, Z. M. Wang, Q. J. Peng, X. Dai, Z. Fang, Z. Y. Xu, C. T. Chen, and X. J. Zhou, Electronic evidence of temperature-induced lifshitz transition and topological nature in ZrTe_5 , *Nature Commun.* **8**, 15512 (2017).
- [23] A. Damascelli, Z. Hussain, and Z. X. Shen, Angle-resolved photoemission studies of the cuprate superconductors, *Rev. Mod. Phys.* **75**, 473 (2003).
- [24] M. R. Norman, H. Ding, M. Randeria, J. C. Campuzano, T. Yokoya, T. Takeuchi, T. Takahashi, T. Mochiku, K. Kadowaki, P. Guptasarma, and D. G. Hinks, Destruction of the Fermi surface in underdoped high-Tc superconductors, *Nature (London)* **392**, 157 (1998).
- [25] S. Martin, A. T. Fiory, R. M. Fleming, L. F. Schneemeyer, and J. V. Waszczak, Temperature Dependence of the Resistivity

- Tensor in Superconducting $\text{Bi}_2\text{Sr}_{2.2}\text{Ca}_{0.8}\text{Cu}_2\text{O}_8$ Crystals, *Phys. Rev. Lett.* **60**, 2194 (1988).
- [26] O. K. Andersen, A. I. Liechtenstein, O. Jepsen, and F. Paulsen, LDA energy bands, low-energy hamiltonians, t' , t'' , $t_{\perp}(\mathbf{k})$ and J_{\perp} , *J. Phys. Chem. Solids* **56**, 1573 (1995).
- [27] A. Bansil, and M. Lindroos, Importance of Matrix Elements in the ARPES Spectra of BISCO, *Phys. Rev. Lett.* **83**, 5154 (1999).
- [28] Y. H. Su, J. Chang, H. T. Lu, H. G. Luo, and T. Xiang, Effect of bilayer coupling on tunneling conductance of double-layer high- T_c cuprates, *Phys. Rev. B* **68**, 212501 (2003).
- [29] T. Hashimoto, Y. Ota, H. Q. Yamamoto, Y. Suzuki, T. Shimojima, S. Watanabe, C. T. Chen, S. Kasahara, Y. Matsuda, T. Shibauchi, K. Okazaki, and S. Shin, Superconducting gap anisotropy sensitive to nematic domains in FeSe, *Nature Commun.* **9**, 282 (2018).
- [30] D. F. Liu, C. Li, J. W. Huang, B. Lei, L. Wang, X. X. Wu, B. Shen, Q. Gao, Y. X. Zhang, X. Liu, Y. Hu, Y. Xu, A. J. Liang, J. Liu, P. Ai, L. Zhao, S. L. He, L. Yu, G. D. Liu, Y. Y. Mao, X. L. Dong, X. W. Jia, F. F. Zhang, S. J. Zhang, F. Yang, Z. M. Wang, Q. J. Peng, Y. G. Shi, J. P. Hu, T. Xiang, X. H. Chen, Z. Y. Xu, C. T. Chen, and X. J. Zhou, Orbital Origin of Extremely Anisotropic Superconducting Gap in Nematic Phase of FeSe Superconductor, *Phys. Rev. X* **8**, 031033 (2018).
- [31] P. J. Hirschfeld, M. M. Korshunov, and I. I. Mazin, Gap symmetry and structure of Fe-based superconductors, *Rep. Prog. Phys.* **74**, 124508 (2011).
- [32] F. Wang, and D. H. Lee, The electron-pairing mechanism of iron-based superconductors, *Science* **332**, 200 (2011).
- [33] K. Kuroki, S. Onari, R. Arita, H. Usui, Y. Tanaka, H. Kontani, and H. Aoki, Unconventional Pairing Originating from the Disconnected Fermi Surfaces of Superconducting $\text{LaFeAsO}_{1-x}\text{F}_x$, *Phys. Rev. Lett.* **101**, 087004 (2008).
- [34] I. I. Mazin, D. J. Singh, M. D. Johannes, and M. H. Du, Unconventional Superconductivity with a Sign Reversal in the Order Parameter of $\text{LaFeAsO}_{1-x}\text{F}_x$, *Phys. Rev. Lett.* **101**, 057003 (2008).
- [35] H. Ding, P. Richard, K. Nakayama, K. Sugawara, T. Arakane, Y. Sekiba, A. Takayama, S. Souma, T. Sato, T. Takahashi, Z. Wang, X. Dai, Z. Fang, G. F. Chen, J. L. Luo, and N. L. Wang, Observation of Fermi-surface-dependent nodeless superconducting gaps in $\text{Ba}_{0.6}\text{K}_{0.4}\text{Fe}_2\text{As}_2$, *Europhys. Lett.* **83**, 47001 (2008).
- [36] D. X. Mou, T. Kong, W. R. Meier, F. Lochner, L. L. Wang, Q. S. Lin, Y. Wu, S. L. Bud'ko, I. Eremin, D. D. Johnson, P. C. Canfield, and A. Kaminski, Enhancement of the Superconducting Gap by Nesting in $\text{CaKFe}_4\text{As}_4$: A New High Temperature Superconductor, *Phys. Rev. Lett.* **117**, 277001 (2016).
- [37] K. Seo, B. A. Bernevig, and J. P. Hu, Pairing Symmetry in a Two-Orbital Exchange Coupling Model of Oxypnictides, *Phys. Rev. Lett.* **101**, 206404 (2008).
- [38] Y. M. Xu, Y. B. Huang, X. Y. Cui, E. Razzoli, M. Radovic, M. Shi, G. F. Chen, P. Zheng, N. L. Wang, C. L. Zhang, P. C. Dai, J. P. Hu, Z. Wang, and H. Ding, Three-dimensional superconducting gap function in optimally doped $\text{Ba}_{0.6}\text{K}_{0.4}\text{Fe}_2\text{As}_2$, *Nature Phys.* **7**, 198 (2011).